[Scanning Microscopy](https://digitalcommons.usu.edu/microscopy)

Volume 5 | Number 4 Article 7

10-9-1991

Scanning Electron Acoustic Microscopy and Scanning Electron Microscopic Imaging of III-V Compounds Devices

J. F. Bresse
FRANCE-TELECOM

Follow this and additional works at: https://digitalcommons.usu.edu/microscopy

Part of the Biology Commons

Recommended Citation

Bresse, J. F. (1991) "Scanning Electron Acoustic Microscopy and Scanning Electron Microscopic Imaging of III-V Compounds Devices," *Scanning Microscopy*: Vol. 5 : No. 4 , Article 7.
Available at: https://digitalcommons.usu.edu/microscopy/vol5/iss4/7

This Article is brought to you for free and open access by the Western Dairy Center at DigitalCommons@USU. It has been accepted for inclusion in Scanning Microscopy by an authorized administrator of DigitalCommons@USU. For more information, please contact digitalcommons@usu.edu.

Scanning Microscopy, Vol. 5, No. 4, 1991 (Pages 961-968)
Scanning Microscopy International, Chicago (AMF O'Hare), IL 60666 USA
0891-7035/91$3.00+.00

SCANNING ELECTRON ACOUSTIC MICROSCOPY AND SCANNING ELECTRON MICROSCOPIC IMAGING OF III-V COMPOUNDS DEVICES

J. F. Bresse*

FRANCE-TELECOM, Centre National d'Etudes des Télécommunications
Laboratoire de Bagneux, groupement PMM, département MPM
196 Avenue Henri Ravera, F-92220 Bagneux, France

(Received for publication April 24, 1991, and in revised form October 9, 1991)

Abstract

Scanning electron acoustic microscopy (SEAM) and SEM infrared imaging (SEMIR) use both a modulated electron beam to generate thermal waves which produce acoustic waves detected by a transducer in the case of SEAM and affect the surface temperature which is directly monitored by the infrared emission. Both techniques are used to visualize non-adherence zones in III-V compounds devices. SEAM is applied to metallic layers like Au, Au-Ti, W-Mo-Ge deposited on a GaAs substrate. SEAM images are correlated with global adherence measurements.

SEMIR is applied to dielectric layers, like Si_3N_4/InP. An estimation of the surface temperature is given. Sensitivity and spatial resolution of both techniques are given and compared.

Key words: Scanning electron acoustic microscopy, infrared thermography, gallium arsenide, indium phosphide, adherence, thin films, gold, titanium, tungsten, silicon nitride.

*Address for correspondence: J.F. Bresse, C.N.E.T., BP 107, 92225 BAGNEUX Cedex, France
Phone No.: 33-1-45 29 52 43
Fax: 33-1-42 53 49 30

Introduction

Scanning Electron Acoustic Microscopy (SEAM) is based on the local thermal excitation of the sample and the detection of the acoustic waves generated in the heated zone due to the thermoelastic properties of the material (Brandis and Rosencwaig, 1980 ; Cargill, 1980). In piezoelectric materials and ionic crystals, piezoelectric coupling has been evoked to explain the results (Kultscher and Balk, 1986 ; Urchulutegui and Piqueras 1990).

SEAM has proved to be a very powerful technique for device failure analysis. Several unique possibilities have been shown, for example, imaging of features under an oxide layer (Rosencwaig and White, 1981), in-depth visualization using either a shift of the detection phase (Brandis and Rosencwaig, 1980 ; Davies, 1983 ; Rosencwaig, 1982) or a boxcar convolution to sample the transient response (Balk and Kultscher, 1984) or by changing the electron beam range (Bresse, 1988, Takenoshita, 1988). Visualization of non-adherence zones between a metallic layer and the semiconductor is also a unique field of application for SEAM. Such zones have been visualized for Au and Au-Ti layers on GaAs (Bresse, 1988, Bresse 1990). Ohmic contacts and Schottky barriers on GaAs, with interface compounds formation, (Bresse, 1988 ; Kirkendall and Remmel 1984) have also been studied.

For SEM infrared imaging (SEMIR), the far infrared light emitted by the periodically heated surface can be collected by an ellipsoïdal mirror and detected by an InSb photodiode which has a wavelength response from 1 to 5 μm. This provides a direct means of monitoring the surface temperature in the region affected by the thermal waves generated by the electron beam. By this way, surface temperature imaging can be obtained. Examples of the use of this technique have been previously demonstrated in bulk glass material (Dacol and Utterback, 1987), for a metal deposited on a silicon nitride layer on a silicon substrate (Dacol et al., 1985) and for a metal deposited on a resin layer (Ermert et al., 1984).

In this paper, we will show examples of the use of both techniques for the study of non-adherence zones. Non-adherence increases the local heating of the deposited layer producing acoustic waves however the presence of an air layer strongly affects the transmission of the acoustic waves to the substrate and to the transducer with the result that the net sign change for the acoustic amplitude is uncertain. SEMIR gives a direct mapping of the increase of temperature in non-adherence zones and allows these effects to be separated. The physics of the phenomena underlying both techniques is presented first. The use of SEAM for the visualization of non-adherences zones in shown in the case of Au, Au-Ti and W-Mo-Ge layers on a GaAs substrate. SEMIR is used to visualize non-adherence zones of silicon nitride deposited on an InP substrate. An

Table 1 : Spatial resolution and main contrast mechanism in SEAM.

Case	Spatial resolution	Main contrast mechanism
$\phi_b/2 < R, \mu < D < \lambda_a$	λ_a	acoustic
$\phi_b/2 < R < D < \mu < \lambda_a$	μ	thermoelastic
$\phi_b/2 < D < \mu < R < \lambda_a$	μ	thermoelastic and electronic
$\phi_b/2 < D < R < \mu < \lambda_a$	R	electronic and thermoelastic
$D < \phi_b/2 < R, \mu < \lambda_a$	ϕ_b	electronic and thermoelastic

evaluation of the surface temperature is given in that case. In the discussion we give an estimation of the sensitivity and the spatial resolution which may be achieved by the two techniques.

SEAM principle, physical phenomena, signal amplitude

SEAM in based on a local excitation of the sample surface by a periodic electron excitation. In metals where the thermal phenomenon is the only contribution, the excitation causes a local periodic heating. The heat diffusion corresponding to this situation can be modeled by the development of a thermal wave which is so much damped that it does not propagate further than one thermal wavelength (λ_T). The solution of the diffusion equation shows that the amplitude of the thermal wave is attenuated by a factor e after a propagation of one thermal diffusion length, μ ($\mu=\lambda_T/2\pi$) expressed as :

$$\mu = \left(\frac{k'}{\pi f}\right)^{1/2} \quad \text{with} \quad k' = \frac{k}{\rho C} \qquad (1)$$

where k is the thermal conductivity, ρ the density, C the specific heat of the material, and f the operating frequency.
The local heating causes a dilatation of the sample giving a stress and a strain which is relaxed through acoustic wave generation. The acoustic wavelength, λ_a, is given by :

$$\lambda_a = v_s \;/\; f \qquad (2)$$

The spatial resolution d_s is governed by the three parameters : beam spot size ϕ_b, electron range R, and the thermal diffusion length :

$$d_s = [\phi_b^2 + R^2 + \mu^2]^{1/2} \qquad (3)$$

Depending of the relative importance of these three parameters and the depth of the observed feature, D, one of these parameters will govern the spatial resolution. In the table 1 the different situations are shown and the main parameters governing the spatial resolution is given (Qian and Cantrell, 1989). In most cases the sample thickness is much less than the acoustic wavelength and the main contrast mechanism is not from acoustic origin. For example at 1 MHz frequency the acoustic wavelength is around 5 mm and most of our samples have a thickness of 300 µm or less.

For the other types of mechanisms evoked to explain the signal generation the main parameter governing the spatial resolution may be the minority carriers diffusion length in the case of the excess carriers mechanism or the electron range in the case of piezoelectric materials.

Signal amplitude In the case of the thermal mechanism, theoretical expressions of the resultant stress for a specimen with a free surface have been given either in the one-dimensional case (White 1963, Opsal and Rosencwaig 1982) or in the three-dimensional case (Holstein 1985, Qian and Cantrell 1989). In this case the output of the transducer can be expressed as :

$$V_{acoust} = R_{trans} \frac{3 \; a_t \; B \; P_0}{(2\pi \; f \; \rho \; C \; k)^{1/2}} \qquad (4)$$

with:

$$R_{trans} = \frac{g_{33} \; l_1}{\pi \; b_1^2} \qquad (5)$$

where :
a_t, linear coefficient of thermal expansion (K^{-1})
B, bulk elastic modulus ($N.\ cm^{-2}$)
P_0, electron beam power (W)
ρ, density ($g.cm^{-3}$)
C, specific heat ($J\ .g^{-1}\ .\ K^{-1}$)
k, thermal conductivity ($W\ .\ cm^{-1}\ .\ K^{-1}$)
g_{33}, transducer piezoelectric voltage constant ($V.cm.N^{-1}$)
πb_1^2, transducer-sample coupling area (cm^2)
l_1, transducer thickness (cm)

In the other signal generation mechanisms no expression have been given yet but the signal may depend on the piezoelectric stress constant and the elastic stiffness constant of the material for the piezoelectric coupling and depends on the minority carrier lifetime, permittivity and the elastic stiffness constant for the excess carrier mechanism (Kultscher and Balk 1986).

Surface temperature, infrared emitted power

Surface temperature estimation. In the case of an isotropic homogeneous target, the heat diffusion can be described by :

$$\nabla^2 T(r,t) = \frac{1}{k'}\frac{\partial T}{\partial t} - \frac{1}{k} F(r,t) \qquad (6)$$

T (r,t) is the space, and time dependent temperature, F (r,t) is a source density function, k', thermal diffusivity ($cm^2.sec^{-1}$) ($k' = k/\rho C$).
The solution of this equation depends of the source function and the boundary conditions.
The temperature may be written as :

$$T(r,t) = T_0 + \theta(r,t) \qquad (7)$$

T_0 is the invariant term, as the ambient temperature, $\theta(r,t)$ is the increase of temperature.
L.G. Pittaway (1964) has treated the case of an electron beam where the power is only absorbed at the surface with a gaussian distribution governed by the spot size, ϕ_b . The surface temperature, θ_s, has its maximum value after a time for steady-state, t_{stat}, which is given by :

$$t_{stat} \sim 40\frac{\phi_b^2}{k'} \qquad (8)$$

and :

$$\theta_s \sim \frac{1}{\pi^{3/2}} \frac{P_0}{k\phi_b} \qquad (9)$$

With a spot size, ϕ_b, of 1 µm, for a metal, with k' = 1 cm²/s, t_{stat} = 0.4 µs, for a semiconductor, with k' = 0.25 cm²/s, t_{stat} = 1.6 µs, for an insulator, with k' = 10^{-2} cm²/s, t_{stat} = 40 µs.
O.C. Wells (1965) has considered the problem in three dimensions, taking into account the fact that the electron beam penetration gives an increase of both the heated depth, Zv, and the heated surface diameter, ϕ_v.

$$\phi_v^2 = \phi_b^2 + \phi_Z^2 + \phi_t^2 \quad (10)$$

$$\phi_Z = 1.117R \quad (11)$$

$$\phi_t = 2.35(k't)^{1/2} \quad (12)$$

$$Z_v^2 = \phi_Z^2 + \phi_t^2 \quad (13)$$

The evolution of the heated volume is determined at the time t_{stat}, when the steady-state is reached :

$$t_{stat} = \frac{0.0615}{k'} \phi_v^2 \quad (14)$$

The final maximum surface temperature is given by :

$$\theta_v = 0.103 \frac{P_o}{k \ Z_v} \quad (15)$$

The maximum surface temperature θ_v, taking into account the electron beam penetration, is in general lower than the value given by the formula (8), obtained by Pittaway.
For example with k' = 1 cm²/s, R = 1 µm, ϕ_b=1µm, t_{stat} ~2.10^{-9} s instead of 0.4 µs. With k' ~10^{-2} cm²/s, R = 4 µm, ϕ_b=1 µm, t_{stat} ~5 µs instead of 40 µs.
Table 2 gives, for several metals, semiconductors and insulators, the calculated values of ϕ_v, Zv, and θ_v (given by Wells formula) for an electron beam of 20 keV and 100 nA, with a spot size of 0.5 µm. The electron range, used for the calculations is given by (Kanaya and Okoyama, 1972):

$$R(\mu m) = \frac{0.276}{\rho} \frac{A}{Z^{8/9}} (E_o)^{5/3} \quad (16)$$

A, atomic weight, Z atomic number, Eo beam energy (keV).

Infrared emitted and detected power. The total infrared power, P_r, radiated from the surface and collected can be calculated by the following relation :

$$Pr(t) = \int\int_{Ar} \varepsilon.\sigma.T^4(r,t)dAr \quad (17)$$

ε, surface emissivity, σ Stefan - Boltzman constant.
If the increase of surface temperature is small as compared to the ambient temperature, we can write :

$$T = T_0\left(1 + \frac{\theta}{T_0}\right) \quad so \quad T^4 \sim T_0^4\left(1 + \frac{4\theta}{T_0}\right) \quad (18)$$

The increase of emitted power, $\Delta P_r(t)$, can be written as :

$$\Delta P_r(t) = 8\pi \ \varepsilon \ \sigma \ T_o^3 \int_{r=o}^{r=\infty} \theta(r,t) \ r dr \quad (19)$$

But in order to take into account the spectral distribution of the emitted power and the detection by a photodiode which has a limited spectral response, we must consider the black-body emissive power, E_b, given by the energy density per wavelength and per unit volume :

$$\mu_\lambda = \frac{8\pi \ hc \ \lambda^{-5}}{e^{hc/\lambda T} - 1} \quad (20)$$

$$E_b = \mu_\lambda c / 4 \quad (21)$$

Table 2. Calculated electron range, R, heated diameter, Φ_v, heated depth, Zv, surface temperature, θ_v, and time for steady-state, tstat, using Wells expressions.

Element	R(µm)	$\Phi_v(\mu m)$	Z_v(µm)	$\theta_v(C)$	$t_{stat}(10^{-8}$ s)
Cu	1.45	2.18	2.12	0.20	0.26
Al	4.14	6.00	5.98	0.13	2.26
Au	0.84	1.35	1.26	0.35	0.09
Mo	1.39	2.10	2.04	0.59	0.50
Ti	2.77	4.04	4.01	2.08	12.6
W	0.84	1.36	1.27	0.65	0.17
Si	4.68	6.77	6.75	0.18	3.13
GaAs	2.54	3.71	3.67	1.00	3.52
InP	2.85	4.15	4.12	0.58	2.40
SiO2	4.78	6.90	6.89	29.6	480
Ge	2.54	3.72	3.68	0.76	2.36

$$E_b = C_1 \lambda^{-5} / [\exp(C_2/\lambda T) - 1] \quad (22)$$

$C_1 = 2 \pi h c^2 = 3.74 \ 10^8$ Watt.µm⁴.m⁻², $C_2 = h c = 1.44 \ 10^4$ µm.K, λ, wavelength expressed in microns, c light velocity.

As, $\exp(C_2/\lambda T) \gg 1$, the infrared power seen by the photodiode is given by :

$$P_{IR} \sim \int_{Ar}\int_{\lambda=2}^{\lambda=5} \xi C_1 \lambda^{-5} \exp(-C_2/\lambda T) dAr d\lambda \quad (23)$$

ξ, detection efficiency of the photodiode. For $2 < \lambda < 5$, we can approximate the efficiency by the relation :

$$\xi = (1 + \lambda) \ / \ 6 \quad (24)$$

The calculation can be done for the ambient temperature by integrating the relation (23). The minimum increase of infrared power ΔP_{IRI}, from one point at a temperature $T_0+\theta$, as compared to a reference point at the temperature T_0 with an emissive infrared power, ΔP_{IR0}, can be calculated as :

$$\Delta P_{IRI}/\Delta P_{IR0} = \exp(C_2\theta/\lambda T_0^2) \quad (25)$$

For a small increase of temperature, and at the maximum of the efficiency of detection, (λ = 5), we can approximate the ratio of infrared power by :

$$\Delta P_{IRI}/\Delta P_{IR0} = 1 + C_2\theta/\lambda T_0^2 = 1 + 2.88 10^3\theta/T_0^2 \quad (26)$$

For example, with T_0 = 300K, θ = 10K and 30K, $\Delta P_{IRI}/\Delta P_{IR0}$ is respectively 1.288 and 1.96.

Adherence problems of metallic overlayers

The deposition of a metallic layer on a glass or a semi-conductor often leads to adherence problems. Two different types of adherence problems may occur :

- poor mechanical adhesion which may be influenced by the substrate preparation, the deposition technique, the presence of an intermediate layer between the metal and the substrate. This adhesion may be tested by a global measurement using a pulling technique.
- debonding of the metallization due to the presence of a bubble between the metal and the semiconductor. The presence of a bubble may affect both the thermal flux and the acoustic wave transmission.

The debonding can be easily detected by SEAM. The thermal waves may be scattered by the substrate surface

increasing the surface temperature of the debonded zone. But in this zone the layer may be free to physically vibrate relative to the substrate. That gives a bad transmission of the acoustic waves. SEAM is also able to visualize the first type of adherence problem, but the corresponding increase of signal is usually very small due to the averaging of the increase of temperature for the total sampled depth equal to the thermal wavelength of the substrate.

SEMIR can detect both types of problem, because the infrared emission corresponds to an increase of the surface temperature. The increase of temperature is more important in the second case.

Au layers deposited by Joule effect evaporation and Au as well as Au-Ti layers deposited by electron beam evaporation have been studied for adhesion properties before and after annealing. Global adhesion measurements are made by a pulling technique using a stud of 0.1 inch diameter. The measurements show a better adhesion in the case of Au layers deposited by electron beam evaporation and a strong increase of the adhesion with an intermediate layer of Ti. An annealing also gives an increase of the adhesion.

SEAM experiments have been performed using a commercial system delivered by CAMBRIDGE TECHNOLOGY LTD (47 A Newnham Road, Cambridge CB3 9EY, ENGLAND). The operating frequency can be varied from 10 kHz to 2 MHz. The samples are directly attached on the transducer itself by mixing a specific glue and aquadag. Samples are usually no greater than 5x5 mm. Since the conversion efficiency is low, especially for semiconductors, the operating parameters for the electron beam are usually : 10^{-7} A, 5-40 keV in order to get a signal for imaging with averaging (time constant 300 µs) by a lock-in-amplifier. The electron beam conditions are usually 20 keV beam energy, 100 - 400 nA beam current and an operating frequency of 200 kHz.

Figure 1 a) shows two bubbles on an evaporated gold layer imaged in the SEI mode for the topographical contrast and in the electron acoustic image (Fig. 1b). The observed contrast in the SEAM image is due to the fact that in presence of the air bubble, the heated metal can freely vibrate, giving a bad transmittion of the acoustic waves to the substrate. As the depth of the observed defect is less than the thermal diffusion length of both materials (14 µm in Au and 6.2 µm in GaAs at 200 kHz frequency) and less the electron range, the spatial resolution is only given by the spot size. The density and the size of the bubbles have been evaluated for the Au and Au-Ti layers. A lower density of bubbles and a decrease in size is observed with the Au-Ti layers. These results correlate well with the global measurements of adherence. A change in surface morphology is also observed for the Au-Ti layers as compared to the Au layers.

Strong adherence problems are also observed for W/Mo/Ge layers deposited on GaAs by electron beam evaporation. Figure 2a) and b) presents such layers imaged in SEI mode and in SEAM mode with a frequency of 100 kHz. Strong positive or negative constrasts are observed on lines which follow the topography of the bubbles. This strong contrast is due to the interference of the thermal waves which are reflected on the substrate. This is the reason why the contrasted lines follow the topography of the bubbles. Figure 3a) b), c) shows the influence of the phase shift between the excitation and the detection on the image contrast. This shows that the lines observed on the SEAM images are shifted as function of the phase corresponding to differences in path of the thermal waves.

Adherence problems of dielectric layers

Due to a poor transmission of the thermal flux in non-adherence zones, an increase of the surface temperature of the overlayer is expected. If this increase of temperature is sufficiently high, it can be detected by the thermal infrared emission. The non-adherence zone can also be observed by this way.

A schematic of the infrared detector/collector apparatus is shown on Figure 4. On our apparatus we use the same collection system for the far infrared emission as for cathodoluminescence experiments. The collector is an ellipsoïdal mirror mounted at the end of a periscope system, designed by OXFORD Instruments (OXFORD Instruments Limited, Eynsham, OXFORD 0X8 1TL, England) which allows the output of the light from the microscope chamber through a CaF_2 window (transmission up to 10 µm). The cooled InSb photodiode used for the infrared emission detection has a Ge window which cuts the emitted wavelength lower than 2 µm. The responsivity of the diode has a peak of 3.5 A/W for $\lambda = 5$ µm, reduced to zero for an upper wavelength and decrease of 50 % for $\lambda = 2$ µm. The diode is fitted to a current amplifier which has a gain of 10^6 V/A. The assembly photodiode-preamplifier has a bandwidth up to 265 kHz which allows an operating frequency compatible with the scanning rate using a time constant of 0.3 ms or 1 ms on the lock-in amplifier. The information on the surface temperature by the infrared emission is restricted to the region where the light is collected by the ellipsoïdal mirror which is around 200 µm in diameter for the surface, but a contribution of the optical IR emission from the depth is also possible when the material is optically transparent for IR wavelength.

Figure 5 a) and b) presents the case of a Si_3N_4 (150 nm) layer deposited on InP (n^+). The electron beam conditions are : 20 keV beam energy, 10 µA beam current. The infrared image is obtained by pulsing the beam at 10 kHz, using the lock-in amplifier with a time constant of 1 ms. The time per line was 240 ms and the frame time 100 s. The mean value of the signal outside the non-adherence zones was 20 µV, small as compared to the noise (about 10 mV). This signal was increased to 40 µV at 1 kHz and 140 µV at 100 Hz. The bubbles which give the non-adherence zones between the dielectric and the substrate are clearly visualized by the infrared image. A strong increase of the signal (20 - 30 mV) is also observed on the particles of dust which are deposited on the dielectric layer.

The spatial resolution of the infrared image is nearly equal to the spot size. This can be explained as previously observed by Dacol and Utterback (1987), because the infrared emitted power is a function of T^4, so a small increase in temperature gives a great increase in the emitted power. This allows restriction of the emitted power in a zone nearly equal or less than the spot size.

Estimation of the surface temperature. The surface temperature of the dielectric layer may be estimated considering that the dielectric has a very small thermal conductivity as compared to the substrate.

Figure 6 shows a model for the temperature distribution versus the depth. Assuming a good thermal contact between the dielectric and the substrate, we can write :

$$k_l \quad (dT/dz)_{z=d} \quad = \quad k_s \quad (dT/dz)_{z=d} \tag{27}$$

k_l, thermal conductivity of the dielectric layer,
k_s, thermal conductivity of the substrate,
d, dielectric layer thickness.
The layer thickness is small and the temperature distribution in the layer is linear so :

$$- \, k_l \; \frac{\theta_0 - \theta_1}{d} \; = \; - \, k_s \; \frac{\theta_1}{\mu_s} \tag{28}$$

$$\theta_0 = \theta_1 \left(1 + \frac{k_s \, d}{k_l \, \mu_s} \right) \tag{29}$$

θ_0, surface temperature,
θ_1, temperature at the interface dielectric-substrate ,
μ_s, thermal diffusion length of the substrate.

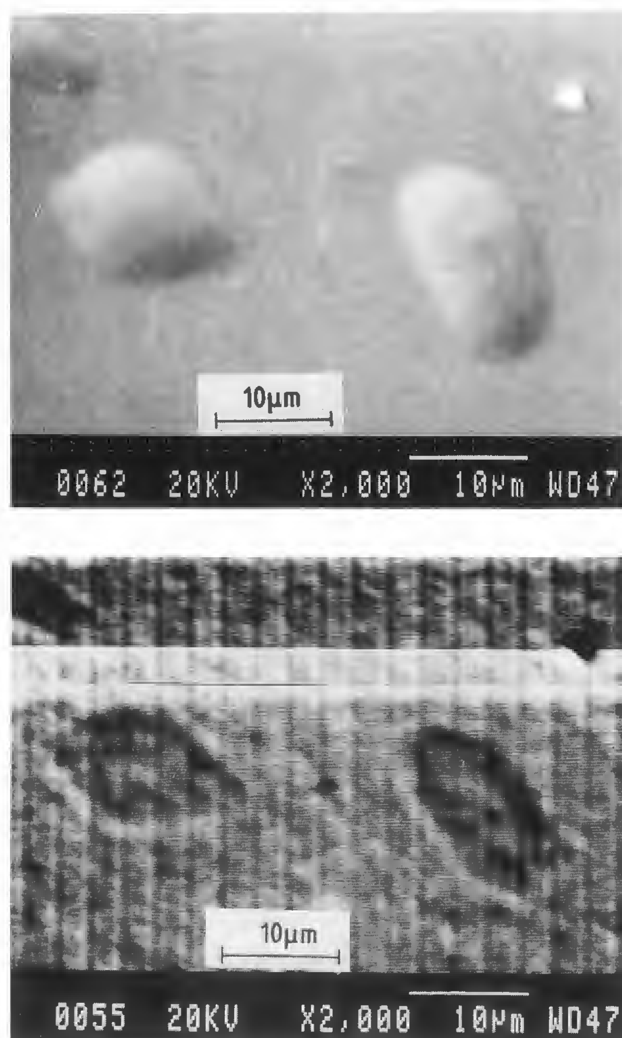

Figure 1: Au (200 nm) deposited on GaAs by Joule effect:
a) secondary electron image
b) scanning electron acoustic image (frequency 200 kHz)

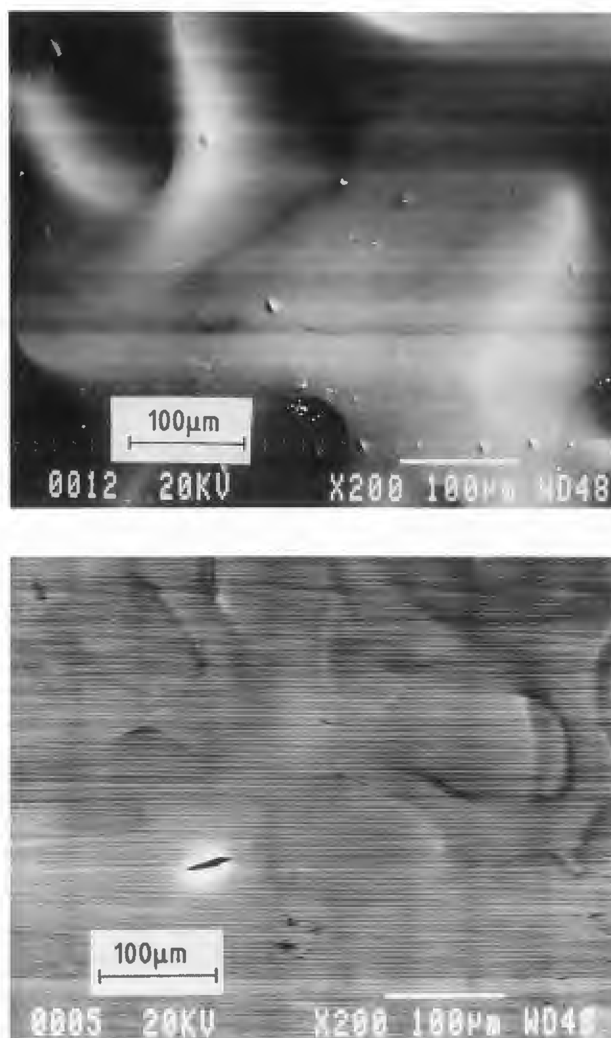

Figure 2: W(300 nm)/Mo(100 nm)/Ge(100 nm) deposited on GaAs by electron beam evaporation
a) secondary electron image (SEI)
b) scanning electron acoustic image (frequency 100 kHz)

Table 3 reports the evolution of the ratio θ_0/θ_1 as function of the frequency, by taking into account the evolution of μ_s and with $k_c = 1.5 \times 10^{-2}$ W.cm^{-1}.K^{-1} and $k_s = 0.71$ W.cm^{-1}.K^{-1}.

The interface temperature is determined by the absorbed power in the layer and in the substrate :

$$\theta_1 = \frac{0.103}{Z_v}\left(\frac{P_l}{k_l} + \frac{P_s}{k_s}\right) \qquad (30)$$

Z_v, heated depth, P_l, absorbed power in the layer, P_s, absorbed power in the substrate.
The heated depth , i.e. 7.05 μm, is obtained after a time corresponding to the steady-state in the nitride layer as given by Wells calculations. The absorbed power in the substrate and in the layer have been evaluated from the value of the mean energy E_1 of electrons at the interface dielectric-substrate and by taking into account the absorption of electrons during their paths by collisions and backscattering.
The energy E_1 is calculated using an approximation of the depth-dose curve (Pouchou, 1989) :

$$\Phi(\rho z) = A\exp(-a\rho z) + [B\rho z + \Phi(0) - A]\exp(-b\rho z) \qquad (31)$$

$$F = \int_0^{\infty} \Phi(\rho z)\,d\rho z = (1 - k\eta)\,\rho\,(1.6 + 0.013Z)\,R \qquad (32)$$

R, electron range, η, backscattering coefficient,

Table 3. Evolution of the ratio θ_0/θ_1 as function of the operating frequency.

Frequency (kHz)	$\mu_s(\mu m)$	θ_0/θ_1
100	12	1.59
10	38	1.19
10	120	1.06
0.1	380	1.02

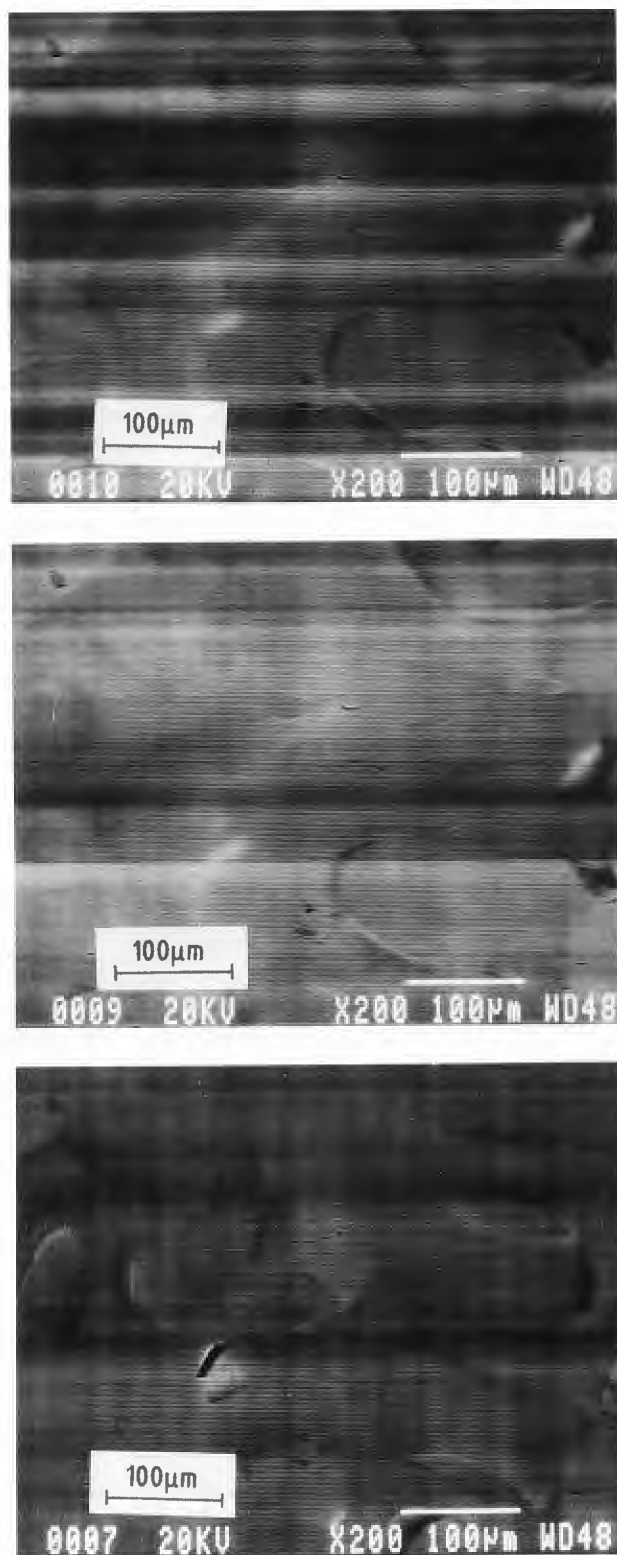

Figure 3: W(300 nm)/Mo(100 nm)/Ge(100 nm) deposited on GaAs by electron beam evaporation
a) SEAM image (frequency 200 kHz, $\Delta\phi=0$)
b) SEAM image (frequency 200 kHz, $\Delta\phi=\pi/4$)
c) SEAM image (frequency 200 kHz, $\Delta\phi=\pi/2$)

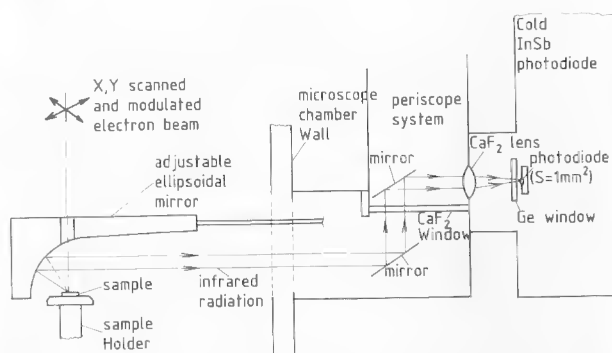

Figure 4: Schematic of the SEM infrared detector/collector appparatus

$$k = 0.45 + 0.002Z \quad (33)$$

The parameters A, B, a, b are determined by knowing ρ, Z and R and by adjusting the shape of the two exponential functions. The intensity variation as a function of the depth is given by (Kanaya and Okoyama, 1972) :

$$I(z/R) = I_0 \exp\left(-\gamma \frac{z/R}{1-z/R}\right) \quad (34)$$

with $\gamma = 0.187 \quad Z^{2/3}$

, I_0, beam intensity.

$$P_s = (1-k_s\eta_s)E_l I(d/R_s) \quad (35)$$

k_s, η_s, R_s are the value of k, η, R of the substrate and $P_l = E_0 I_0 - P_s$.

For the Si_3N_4 (150 nm)/InP case we obtain, for Eo = 20 keV, E_l = 10.14 keV. With I_0 = 10 μA, P_l = 17.7 mW, P_s = 148 mW, θ_l = 195 °C. So for a frequency of 100 Hz, 1 kHz and 10 kHz, θ_0 is respectively 199, 207, 232 ° C.

Discussion

As previously observed (Dacol and Utterback, 1987), the contrast observed for a non-adherence zone is reversed between the SEAM image and the SEMIR image. This is due to the increase of surface temperature of the non-adherence zone as compared to the adherent layer.

For our set-up, the infrared imaging technique is only applicable to dielectric overlayers or to metallic layers deposited on a dielectric layer.

The infrared emission goes as the fourth power of the local temperature, so the spatial resolution, in infrared imaging, is strictly limited to the spot size and a part of the thermal diffusion length (μ/4) of the emitting material (Dacol and Utterback, 1987). This is equal for a dielectric layer, which has a thermal diffusity of 10^{-2} cm^2 sec^{-1}, to 1.25 μm at 10 kHz frequency which is small as compared to the spot size due to high beam current conditions.

For bulk materials, the spatial resolution is better for SEMIR than for SEAM where the spatial resolution is mainly governed by the thermal diffusion length. But in the case of layers, the spatial resolution in SEAM may be limited by the spot size or the electron range if the layer thickness is less than the substrate diffusion length or the beam range (see Table 1).

With our actual apparatus, SEAM can be performed with a beam current ten times lower than for SEMIR, but the signal is more difficult to interpret due to the convolution of both thermal and elastic properties of the heated zone which may correspond to the layer and the substrate. In addition, thermal and elastic properties of the layer may differ from their bulk

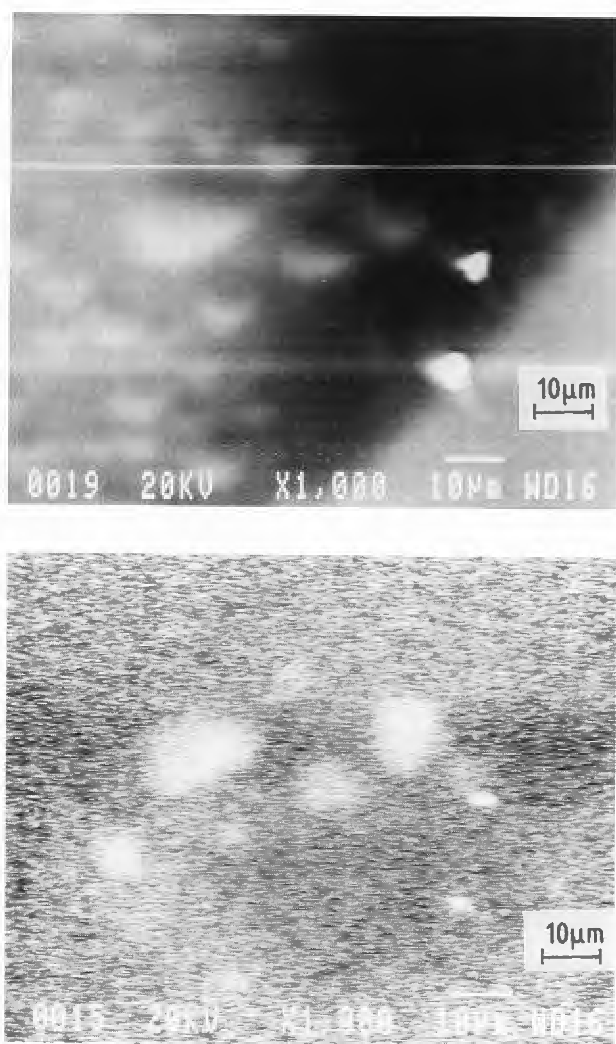

Figure 5: Si_3N_4 (150 nm) InP (n+)
a) secondary electron image (SEI)
b) SEM infrared image (SEMIR)

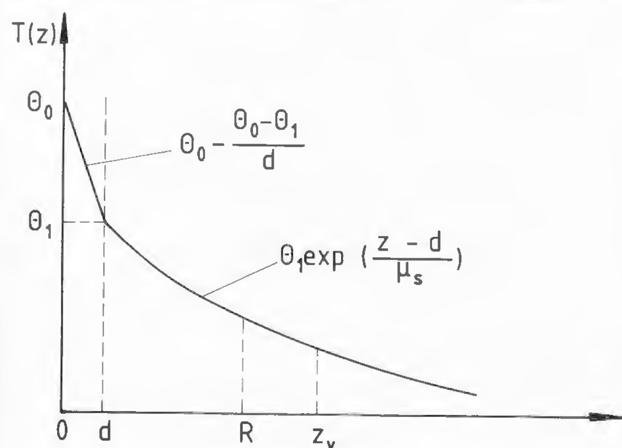

Figure 6: Model of temperature repartition versus depth for the structure dielectric layer/substrate

value, especially for elastic properties in the case of internal stress.

For infrared imaging, the detected radiation may come from the depth if the material is transparent, this in fact may reduce the spatial resolution but may gives also the possibility to visualize in-depth features. This may also explain the increase of the detected signal in the case of the silicium nitride on InP when the frequency is reduced.

Conclusion

Both scanning electron acoustic microscopy and SEM infrared imaging can be used as parallel techniques for the visualization of non-adherence zones. In the actual state, infrared imaging is limited to dielectric layers or to metallic layers deposited on a dielectric. For small thickness layers (≤ 1 μm), both techniques have a comparable spatial resolution, essentially governed by the spot size.

Other applications of both techniques are possible in circuits with complementary informations on local thermal and elastic properties.

References

Balk LJ, Kultscher N (1984). Scanning electron acoustic microscopy with subnanosecond time resolution. J. Physique 45, C2, 873-876.

Brandis E, Rosencwaig A (1980). Thermal wave microscopy with electron beams. Appl. Phys. Lett. 37, 98-100.

Bresse JF (1990). Use of the scanning electron acoustic microscopy (SEAM) for the study of III-V compounds semi-conductors. Scanning, 12, 308-314.

Bresse JF (1988). Scanning electron microscopy studies of III-V compounds : epitaxial layers and devices. Scanning Microsc. 2, 2, 813-819.

Cargill III GS (1980). Ultrasonic imaging in a scanning electron microscope. Nature 286, 691-693.

Dacol FM, Ermert M, Melcher RL (1985). Advances in non-contact thermal-wave imaging with infrared detection. Scanning Electron. Microsc. 1985 ; II : 627-630.

Dacol FM, Utterback S (1987). Parallel acoustic/infrared imaging of single crystal surface and subsurface structure. Scanning Microsc. 1, 3, 1045-1054.

Davies G (1983). Scanning electron acoustic microscopy. Scanning Electron. Microsc. 1983 ; III : 1163-1176.

Ermert M, Dacol FM, Melcher RL, Bauman T (1984). Non contact thermal-wave imaging of subsurface structure with infrared detection. Appl. Phys. Lett. 44, 12, 1136-1138.

Holstein WL (1985). Image formation in electron thermoelastic acoustic microscopy. J. Appl. Phys. 58, 2008-2021.

Kanaya K, Okoyama S (1972). Penetration and energy loss theory of electrons in solid targets. J. Phys. D, 3, 43-58.

Kirkendall TD, Remmel TP (1984). Thermal wave imaging of GaAs material and devices. J. Physique 45, C2, 877-880.

Kultscher N, Balk LJ (1986). Signal generation mechanisms in scanning electron acoustic microscopy. Scanning Electron. Microsc. 1986 ; I : 33-43.

Opsal J., Rosencwaig A. (1982). Thermal wave depth profiling : theory. J. Appl. Phys. 53, 4240-4246.

Pittaway LG (1964). The temperature distribution in thin foil and semi-infinite targets bombarded by an electron beam. Brit. J. Appl. Phys. 15, 967-982.

Pouchou JL (1989). Modèles de correction pour la microanalyse X quantitative. In, ANRT Ed. Microanalyse par sonde électronique : aspects quantitatifs. ANRT, 101 Avenue R. Poincaré 75116 PARIS-FRANCE.

Qian M, Cantrell JH (1989). Signal generation in scanning electron acoustic microscopy. Mater. Sci. Eng. A122, 57-64.

Rosencwaig A, White RM (1981). Imaging of dopant regions in silicon with thermal wave electron microscopy. Appl. Phys.

Lett. 38, 165-167.
Rosencwaig A (1982). Thermal wave imaging. Science. 218, 223-228.
Takenoshita H (1988). The range of observable depth in a pnp Si Darlington Tr-chip by electron acoustic microscopy. Jap. J. Appl. Phys. 27, 1812-1818.
Urchulutegui M, Piqueras J (1990). Signal generation mechanisms in scanning electron acoustic microscopy of ionic crystals. J. Appl. Phys. 67, 1-4.
Wells OC (1965). Calculations of the heat-affected zone during pulsed electron beam machining. IEEE Trans. Electron. Devices ED12, 4, 224-231.
White RM (1963). Generation of elastic waves by transient surface heating. J. Appl. Phys. 34, 3559-3567.

Discussion with Reviewers

J.Holstein : In SEMIR, does the difficulty in distinguishing between variations in the surface temperature T and the emissivity ε limit the practical utilization of the technique for the analysis of more complex device structures?
Author : For more complex device structures, two factors has to be taken into account : the difference in emissivity of the layers, the depth of detection of the infrared emission (i.e. metallic layers are not transparent to the IR emission, but semiconductor or dielectric layers are transparent). These two factors may limit the use of SEMIR, but in my opinion, these effects may be negligible for the detection of hot spots or for zones where the variations in thermal conductivity can strongly influence the surface temperature.

J.Holstein : Some of the contrast observed in the SEI image (Figure 5 a, lower left hand corner), which is suggestive of non-adherence regions, is not observed in the SEMIR image (Figure 5 b). Why do some of the non-adherence regions show up more clearly by SEMIR than others?
Author : The difference in signal between non-adherence regions and regions with adherence is only a factor 2. This may correspond to a difference in temperature of only 30 K. For others regions, where the increase of surface temperature is smaller, the infrared emitted power increase is small and not separated from the noise.
J.C.Murphy : In the section **Adherence problems of dielectric layers,** it is assumed that emission occurs only from the surface. This need not be true for dielectrics where IR emission depth can be large. If emission occurs within the bulk of the specimen the theory underlying detection of disbonding changes from that outlined previously in the paper and a more complete analysis of heat flow, IR emission and adherence is needed. Can the author comment?
Author : It is true that IR emission can be detected not only from the surface but also from the depth in the case of a dielectric layer which is transparent to the infrared emission. This should be not true for metallic layers. The theory underlying the infrared emission should be modified in the following. In the case of a dielectric layer in contact with the semiconductor, the depth of the infrared emission may be limited to $\mu_s/4$ (μ_s, thermal diffusion length of the semiconductor) and more limited in depth in the case of a disbonding due to the increase of temperature of the surface.

L.J.Balk : Some of your SEAM results look similar to spatial derivations of the secondary images (see for instance Fig.1 a and b). Is there any explanation for this phenomenon?
Author : On the Fig.1 b, the observed increase of signal at the limit of the debonded area is not due to a spatial derivation of the secondary electron image but corresponds to an increase of absorbed power due to the metal curvature. The same phenomenon has been more clearly observed on more spherical bubbles on Au layers on GaAs (Bresse 1990).
L.J.Balk : Can you comment on the spatial resolution you achieve with your techniques? Is there a chance of improving them?
Author : SEAM spatial resolution is dependent on the depth of the feature. When the feature depth is less than the beam penetration or the beam size, the spatial resolution may be improved by adjusting the beam parameters, essentially reducing the beam size. This could be possible by improving the electronic of detection. The other factor which influences the spatial resolution is the frequency which governs the thermal diffusion length. Higher frequency may be used to pulse the electron beam but other transducers may be used which are less sensitive (a factor 10 or 100) as PZT transducers.

SEMIR has a better spatial resolution than SEAM due to the increase of infrared emitted power as function of T^4. Its spatial resolution is nearly limited to the spot size and an improvement can be obtained by improving the electronic of detection which also increase the temperature sensitivity.
L.J.Balk : How do you define a good thermal contact and how does it differ from a solely good mechanical contact? Did you consider thermal discontinuities, such as changes of thermal impedances, too?
Author : Good mechanical contacts and good thermal contacts are not necessarly related. A good mechanical contact may be achieved by the substrate preparation or the presence of an intermediate layer which may not have a good thermal conductivity. In our models, we do not consider a thermal resistivity at the interface but 2 or 3 dimensional calculations could be made for this case.